

Oxidized and Reduced *Azotobacter vinelandii* Ferredoxin I at 1.4 Å Resolution: Conformational Change of Surface Residues without Significant Change in the [3Fe-4S]⁺⁰ Cluster^{†,‡}

C. G. Schipke, D. B. Goodin, D. E. McRee, and C. D. Stout*

Department of Molecular Biology, The Scripps Research Institute, 10550 North Torrey Pines Road, La Jolla, California 92037-1093

Received December 22, 1998; Revised Manuscript Received May 5, 1999

ABSTRACT: The refined structure of reduced *Azotobacter vinelandii* 7Fe ferredoxin FdI at 100 K and 1.4 Å resolution is reported, permitting comparison of [3Fe-4S]⁺ and [3Fe-4S]⁰ clusters in the same protein at near atomic resolution. The reduced state of the [3Fe-4S]⁰ cluster is established by single-crystal EPR following data collection. Redundant structures are refined to establish the reproducibility and accuracy of the results for both oxidation states. The structure of the [4Fe-4S]²⁺ cluster in four independently determined FdI structures is the same within the range of derived standard uncertainties, providing an internal control on the experimental methods and the refinement results. The structures of the [3Fe-4S]⁺ and [3Fe-4S]⁰ clusters are also the same within experimental error, indicating that the protein may be enforcing an entatic state upon this cluster, facilitating electron-transfer reactions. The structure of the FdI [3Fe-4S]⁰ cluster allows direct comparison with the structure of a well-characterized [Fe₃S₄]⁰ synthetic analogue compound. The [3Fe-4S]⁰ cluster displays significant distortions with respect to the [Fe₃S₄]⁰ analogue, further suggesting that the observed [3Fe-4S]⁺⁰ geometry in FdI may represent an entatic state. Comparison of oxidized and reduced FdI reveals conformational changes at the protein surface in response to reduction of the [3Fe-4S]⁺⁰ cluster. The carboxyl group of Asp¹⁵ rotates ~90°, Lys⁸⁴, a residue hydrogen bonded to Asp¹⁵, adopts a single conformation, and additional H₂O molecules become ordered. These structural changes imply a mechanism for H⁺ transfer to the [3Fe-4S]⁰ cluster in agreement with electrochemical and spectroscopic results.

Iron–sulfur ([Fe–S]) cluster-containing proteins participate in electron transfer, catalytic, regulatory, and structural functions (1–3). Electron-transfer reactions involving [Fe–S] clusters occur in small proteins containing 1, 2, 3, 4, 7, or 8 Fe atoms in one or more clusters or centers in rubredoxins (Rds),¹ ferredoxins (Fds), and high-potential iron proteins (HiPIPs) (2, 4) and in larger multidomain complexes, such as chloroplast cytochrome *b₆f* (5). Biologically relevant redox couples occur for Fe^{3+/2+}(Sγ)₄ Rd centers, [4Fe-4S]^{3+/2+} clusters in HiPIPs, and [4Fe-4S]^{2+/+} and [2Fe-2S]^{2+/+} clusters in Fds; reduction potentials range from –650 mV in [4Fe-4S]^{2+/+} Fd clusters to +350 mV in HiPIPs (1). The protein matrix influences cluster reduction potential by controlling solvent accessibility and the number of amide dipoles directed at μ₂-S, μ₃-S cluster and Sγ ligand atoms (6). The protein may further influence reduction potential

by enforcing an ‘entatic’ or ‘rack’ state, restraining [Fe–S] cluster structure intermediate between ground-state oxidized and reduced geometries (7, 8). In blue copper proteins, for example, this effect raises the reduction potential by enforcing distorted tetrahedral geometry on the Cu(I) site and restricting the approach of an axial Met ligand in both the Cu(I) and Cu(II) states; structural reorganization between the oxidized and reduced states is therefore minimized, enhancing the rate of electron transfer (9).

Structural characterization of [Fe–S] proteins in both oxidized and reduced states has been limited. In the MoFe protein of nitrogenase, a Ser side chain and a main chain N ligand in the oxidized cluster, P^{ox}, are exchanged for two new Fe–S bonds in the reduced state, Pⁿ (10). Concomitant with this structural change, a significant expansion occurs in the Pⁿ cluster relative to the P^{ox} cluster as manifested in a 0.15 Å longer average Fe–Fe distance (11). Initial comparison of the structures of *Peptococcus aerogenes* 8Fe Fd and *Chromatium vinosum* HiPIP lead to the observation that protein-bound [4Fe-4S]^{2+/+} clusters can exhibit the [4Fe-4S]^{2+/+} redox couple, as in Fds, or the [4Fe-4S]^{3+/2+} couple, as in HiPIPs (12). In *C.v.* HiPIP the reduced [4Fe-4S]^{2+/+} cluster manifests longer Fe–S bonds (~0.1 Å), resulting in a tetragonal distortion of the cluster, and shorter (~0.2 Å) NH···S interactions (13). In contrast, oxidized and reduced *Pyrococcus furiosus* Rd structures refined at 1.8 Å resolution show smaller increases in the Fe–Sγ bond lengths (0.04 Å)

[†] This work supported by the National Institutes of Health (Grant GM48495 to D.B.G. and D.E.M. and Grant GM36325 to C.D.S.).

[‡] Coordinates and structure factors for three new, refined ferredoxin structures have been deposited with the Protein Data Bank (Ox2, Red1, and Red2; accession codes 7FD1, 6FDR, and 7FDR, and r7fd1sf, r6fdrsf and r7fdrsf, respectively).

* To whom correspondence should be addressed: Phone: 619-784-8738. Fax: 619-784-2857. E-mail: dave@scripps.edu.

¹ Abbreviations: FdI, *Azotobacter vinelandii* 7Fe ferredoxin; [2Fe-2S], [3Fe-4S], and [4Fe-4S], protein-bound [Fe–S] clusters; [Fe₂S₂], [Fe₃S₄], and [Fe₄S₄], core structures in synthetic [Fe–S] cluster analogue compounds; Rd, rubredoxin; Fd, ferredoxin; HiPIP, high-potential iron protein; *su*, standard uncertainty; EPR, electron paramagnetic resonance.

and smaller decreases in the NH⁺⋯S interactions (0.09 Å) upon reduction (14). Structures of oxidized and dithionite-reduced *Azotobacter vinelandii* 7Fe ferredoxin (FdI) at pH 8 and pH 6 determined at 2.2–1.9 Å resolution indicate apparent shifts within the [3Fe-4S]⁺⁰ cluster and a conformational change of Asp¹⁵, a surface residue proximal to this cluster (15).

Synthetic inorganic analogues provide an essential reference for understanding how proteins select, influence, or control the properties of inorganic [Fe-S] centers (3). Synthetic inorganic complexes have been characterized at atomic resolution as analogues of [2Fe-2S], [3Fe-4S], and [4Fe-4S] protein-bound clusters (1). These include a large number of compounds with thiolate ligands and [Fe₂S₂]^{2+/1+} and [Fe₄S₄]^{2+/1+} cores (16) as well as trinuclear cuboidal and heterometallic cubane clusters (17, 18). The synthesis of a [3Fe-4S] cluster analogue in the reduced state, [Fe₃S₄]⁰, has been accomplished (19). The synthetic [Fe₃S₄]⁰ cluster has electronic, magnetic, and structural properties in accord with protein-bound [3Fe-4S] clusters (19).

Recently the use of cryocrystallography techniques and synchrotron radiation has allowed very high (~1.0 Å) resolution data to be collected from protein crystals (20). At this resolution, the observation-to-parameter ratio allows refinement of the protein structure with anisotropic temperature factors and without the use of geometric restraints (21). This methodology can be applied to metalloproteins at somewhat lower resolution (~1.5 Å). In this case, longer metal–ligand bond lengths allow unrestrained refinement of metal and inorganic sulfur atoms while restraints are applied to the protein component of the structure. Inversion of the full-matrix of positional shifts at the end of refinement results in standard uncertainty (*su*) values for the heavy atoms that are unbiased by geometric restraints. Application of this method to oxidized FdI at 1.35 Å resulted in *su* values of 0.01 Å for Fe–S bonds in the [3Fe-4S]⁺ and [4Fe-4S]²⁺ clusters (22). Two other [Fe-S] proteins refined in this manner are *Clostridium acidurici* Fd, which contains two [4Fe-4S]²⁺ clusters (23), and *Pyrococcus furiosus* Rd, which contains an Fe³⁺(Sγ)₄ center (24). In the Fd case, data were collected to 0.94 Å resolution, and the *su* values for Fe–S bonds are ≤0.003 Å; in the Rd case, data were collected to 0.95 Å, and the *su* values for Fe–S bonds are also ≤0.003 Å. In one other case, the structure of *Desulfovibrio gigas* Fd, which contains a [3Fe-4S]⁺ cluster, was refined at 1.7 Å resolution, resulting in *su* values for Fe–S bonds of ~0.05 Å (25). However, in no case has an [Fe-S] protein structure been refined at ≤1.5 Å resolution for more than one oxidation state of the [Fe-S] cluster.

Azotobacter vinelandii FdI is an extensively studied [Fe-S] protein that provides a model system for addressing basic questions about [Fe-S] cluster structure and function (26–31). FdI contains 106 residues including 9 Cys, 3 as ligands to the [3Fe-4S]⁺⁰ cluster, 4 as ligands to the [4Fe-4S]^{2+/+} cluster, and 2 nonligand Cys, 1 proximal to each cluster (22, 32). The reduction potential of the [4Fe-4S]^{2+/+} cluster is –650 mV; that of the [3Fe-4S]⁺⁰ cluster is –420 mV at pH 7.8 but is also strongly pH dependent (33). The [Fe-S] clusters in FdI have been characterized by Mössbauer, MCD, CD, and EPR spectroscopies (34, 35) and employed to evaluate the effects of ferricyanide oxidation (36). The physiological electron-transfer partner of FdI has been

identified and characterized as a FAD-containing NADPH:ferredoxin reductase (FPR) (37–39) and shown to be a component of an oxidative stress response pathway in *A. vinelandii* (40–42).

FdI provides a well-characterized example of redox-gated H⁺ transfer in a [Fe-S] protein. The FdI [3Fe-4S]⁺⁰ cluster exhibits a pH-dependent reduction potential and reversible protonation in the reduced state (43–45). Electrochemical, mutagenesis, and spectroscopic experiments have established that upon reduction of the [3Fe-4S]⁺ cluster, Asp¹⁵, a residue on the protein surface directly adjacent to the cluster, facilitates rapid translocation of a H⁺ to the [3Fe-4S]⁰ cluster. Protonation is presumed to occur at the nearest μ₂S atom via conformational change of Asp¹⁵ to form [3Fe-4S]⁰-H⁺. The pK_a of the [3Fe-4S]⁰ cluster is 7.8 when Asp¹⁵ is ionized and 6.5 when Asp¹⁵ is protonated (45). Thus, the FdI system provides a model for a redox-driven proton pump in the forward direction; reoxidation of the cluster requires that the H⁺ first be released (45).

In this paper the refined structure of reduced FdI at 1.4 Å resolution is reported, permitting for the first time direct comparison of [3Fe-4S]⁺ and [3Fe-4S]⁰ clusters in the same protein at atomic resolution. The reduced state of the [3Fe-4S]⁰ cluster is established by single-crystal EPR following data collection. The [4Fe-4S]²⁺ cluster in FdI is not reduced under the conditions used. The structure of the FdI [3Fe-4S]⁰ cluster allows direct comparison with the structure of the [Fe₃S₄]⁰ synthetic analogue, providing insight into the geometric features of the [Fe-S] cores intrinsic to the inorganic entity vs those influenced by the protein structure. Comparison of oxidized and reduced FdI at 1.4 Å reveals conformational changes in the protein relevant to the mechanism of H⁺ transfer to the [3Fe-4S]⁰ cluster.

EXPERIMENTAL PROCEDURES

Crystallization. Tetragonal crystals were grown under aerobic conditions using recombinant protein (33) as described (26, 32). Square bipyramidal crystals approximately 0.4 mm in size in each dimension were chosen for data collection. Crystals were stabilized and transferred in a synthetic mother liquor of 4.8 M (NH₄)₂SO₄ in 150 mM Tris·HCl, pH 8.5.

Data Collection. Four high-resolution data sets have been collected from FdI crystals, two from oxidized crystals (denoted Ox1 and Ox2) and two from reduced crystals (denoted Red1 and Red2) (Table 1). Oxidized refers to the [3Fe-4S]⁺ state, and reduced refers to the [3Fe-4S]⁰ state of FdI. The Ox1 data set corresponds to the 1.35 Å data previously collected at a synchrotron beam line (PDB accession code 6FD1) (22). The crystal used for that experiment was not exposed to reducing agents at any time.

Three new data sets have been collected at 100 K using a rotating-anode X-ray generator and multiwire area detector (Table 1). For the Ox2 data set, an oxidized single crystal was transferred from a 100 μL droplet of synthetic mother liquor into a 50 μL droplet of synthetic mother liquor containing 25% v/v glycerol. After 15 s, the crystal was transferred to a nylon loop and flash-frozen in a cold stream of N₂ gas at 100 K. For the Red1 and Red2 data sets, two single crystals were reduced and frozen inside an anaerobic

Table 1: Data Collection Statistics

data set ^a	oxidized 1 (Ox1)	oxidized 2 (Ox2)	reduced 1 (Red1)	reduced 2 (Red2)
Space Group $P4_12_12$				
unit cell parameters				
<i>a</i> (Å)	54.84	54.46	54.74	54.51
<i>b</i> (Å)	54.84	54.46	54.74	54.51
<i>c</i> (Å)	92.64	92.65	93.77	93.54
wavelength (Å)	1.08 ^b	1.54 ^c	1.54 ^c	1.54 ^c
detector ^{b,c}	Mar	Xen	Xen	Xen
detector settings	14 cm, 29 cm	2θ: 10°, 45°, 50°	2θ: 10°, 45°	2θ: 10°, 45°
max resolution (Å)	1.35	1.30	1.40	1.40
no. of observations	188796	122037	109499	66520
redundancy	3.30 ^d	3.45 ^e	4.56 ^e	2.28 ^e
unique reflections	57315	29311	24027	17496
overall completeness (%)	96.5	82.8	82.8	60.1
avg <i>I</i> / σ (<i>I</i>)	21.3	17.9	13.6	15.4
<i>R</i> _{symm} (<i>I</i>)	0.057	0.082	0.104	0.065
completeness to 1.6 Å (%)	99.1	99.3	91.7	71.1
completeness to 1.4 Å (%)	99.0	95.6	82.8	60.1
last shell				
resolution (Å)	1.45–1.35	1.40–1.30	1.50–1.40	1.50–1.40
completeness (%)	90.3	51.5	55.3	29.8
avg <i>I</i> / σ (<i>I</i>)	1.9	0.82	0.90	1.1
<i>R</i> _{symm} (<i>I</i>)	0.73	0.34	0.44	0.31

^a A single-crystal frozen at 100 K was used for each data set. ^b Data were collected at Stanford Synchrotron Radiation Laboratory beam line 7–1 using a Mar Research 30 cm image plate detector (22). ^c Data were collected using a Siemens direct-drive rotating-anode X-ray generator operated at 55 kV, 90 mA, graphite monochromator, and a Siemens Hi-Star area detector. ^d Data processed in point group 422. ^e Data processed in point group 4/*mmm*.

chamber. For each experiment, a single crystal was transferred to 50 μ L of degassed synthetic mother liquor containing 5 mM sodium dithionite (Na₂S₂O₄, 83% pure) and 85 μ M methyl viologen. After soaking for 30 min, the crystal was transferred to a 50 μ L droplet of synthetic mother liquor containing 25% v/v glycerol, 50 mM Na₂S₂O₄, and 85 μ M methyl viologen. After 15 s, the crystal was transferred to a nylon loop and flash-frozen by immersion in liquid N₂. The blue color of reduced methyl viologen was used as an indicator of the absence of O₂ in the solutions. The high concentration of Na₂S₂O₄ in the cryoprotectant solution was required to destroy oxidants present in the glycerol, as determined by trial EPR measurements using single crystals. Reduced crystals were removed from the glovebox under liquid N₂ and transferred into the 100 K N₂ gas stream (Oxford Cryosystems) on the area detector using precooled steel tongs.

The Ox2, Red1, and Red2 data sets were collected at 100 K using CuK α radiation from a Siemens SRA rotating-anode X-ray generator operated at 55 kV, 90 mA and equipped with a graphite monochromator. The data were recorded with a Siemens Hi-Star area detector mounted on a 3-circle goniometer using two passes with appropriate frame widths and exposure times to accommodate the high- and low-resolution data. In the first pass, the detector angle (2θ) was 10°, the frame width ($\Delta\omega$) was 0.25°, and the exposure time was 1–2 min per frame. A total rotation range of 240° was collected in 4 ω sweeps of 60° at ϕ settings of 0°, 45°, 90°, and 135°. For the high-resolution pass, the detector 2θ was 45°, the frame width ($\Delta\omega$) was 0.1°, and the exposure time was 5–7 min per frame. A total rotation range of 240° was collected in 4 ω sweeps of 60° at ϕ settings of 0°, 45°, 90°, and 135° as for the low-resolution data. For the Ox2 data set, the detector 2θ was set to 50° for one of the 60° ω sweeps. The total time for data collection from each crystal

was 10–14 days. No decay in the diffraction pattern was apparent in this time. The data were indexed, integrated, merged, and scaled using the Xengen suite of programs (46) (Table 1).

EPR. The crystals used for the Ox2 and Red1 data sets were frozen on a nylon loop attached to specialized pins constructed from Bakelite or Lucite. This allowed insertion of the crystal and pin into the X-band microwave cavity of the EPR spectrometer. The pins could be attached to the standard magnetic goniometer supports for X-ray data collection and then transferred from the 100 K N₂ gas stream to liquid N₂ in preparation for EPR. In this manner, the crystals could be kept frozen throughout X-ray data collection, stored in liquid N₂ if necessary, and then used to record EPR spectra. Under liquid N₂, the pin containing a crystal was inserted onto the open end of a 3 mm quartz EPR tube and glued in place with 2-propanol. EPR spectra were recorded at 7 K using a Bruker EMX spectrometer operating at X-band and equipped with an Air Products APD liquid helium cryostat. Spectra were recorded at a microwave frequency of 9.556 GHz and 1 mW power using phase-sensitive detection at 100 kHz field modulation and 5 G amplitude. Digital signal conversion parameters included a 41 ms conversion time, 81 ms time constant, and 5.02×10^3 receiver gain. Initial studies established that these microwave power levels were nonsaturating. The approximate height for optimum positioning within the microwave cavity was established before mounting. For each crystal, the signal amplitude was optimized by fine adjustment of crystal height and rotation about the EPR tube axis. The EPR signal from oxidized single crystals of FdI was observed to have a small orientational anisotropy relative to their broad intrinsic line width. This fact allowed reproducible signals to be obtained and compared by the above rough orientational positioning procedure.

Table 2: Refinement Statistics

structure	oxidized 1 (Ox1)	oxidized 2 (Ox2)	reduced 1 (Red1)	reduced 2 (Red2)
resolution (Å)	1.35–∞	1.30–∞	1.40–∞	1.40–∞
no. of observations	30880	28183	22762	16282
no. of H ₂ O molecules ^a	162	138	144	141
no. of parameters ^{b,c}	9211	8995	8990	9013
data:parameter ratio	3.35	3.13	2.53	1.81
goodness of fit ^d	1.69	2.54	1.97	2.38
R-factor (all data) (%)	15.0 ^e	15.8	17.5	17.0
R-factor ($I > 4\sigma(I)$) (%)	13.8 ^e	13.6	15.0	14.8
average isotropic B , Å ² ^f				
protein C,N,O,S atoms	25.8	16.0	16.6	17.2
cluster Fe,S atoms	19.8	10.4	10.7	12.0
solvent O atoms	43.5	30.5	30.6	30.8
rms deviations				
protein bond lengths (Å)	0.011	0.010	0.008	0.007
protein bond angles (deg)	2.24	2.21	2.01	1.90

^a H atoms not modeled on solvent molecules. ^b Each model includes 841 C, N, O, and S protein, 776 H, 7 Fe, and 8 inorganic S atoms. Lys⁸⁴ refined in two conformations of occupancies 0.35 and 0.65 in the Ox1 structure, and 0.32 and 0.68 in the Ox2 structure. ^c Each structure refined with anisotropic thermal factors for C, N, O, S, Fe atoms and with isotropic thermal factors for H atoms. ^d Goodness of fit: $\{\sum[w(F_o^2 - F_c^2)^2]/(n - p)\}^{1/2}$ where n = no. of reflections, p = no. of parameters. ^e Reference 22. ^f The larger effective isotropic B -factors for the Ox1 structure vs the Ox2, Red1, and Red2 structures may be due to the different area detectors, relative beam intensities, data collection times, and/or scaling procedures used in the two types of experiments.

Structure Refinement and Analysis. The protein structures refined against Ox1, Ox2, Red1, and Red2 data sets (Table 1) are referred to with the same nomenclature as the data sets (Table 2). The Ox2, Red1, and Red2 structures of FdI were refined using the same methodology as reported for the refinement of the Ox1 structure (22). This entailed application of the program Shelx-97 (21) for both conjugate gradient least-squares refinement and block diagonal full-matrix least-squares standard uncertainty analysis. All data, including negative intensities, were used in the refinement. No data were omitted to calculate R_{free} for the Ox2, Red1, and Red2 structures because they were expected to be very similar to the known Ox1 structure. Throughout the refinement calculations, no restraints were applied to bond lengths and angles involving [Fe-S] cluster and S γ ligand atoms. Protein bonds and angles were given target values defined by Engh and Huber (47) and were restrained using σ values of 0.02 Å for bonds and 0.04 Å for angles, where the angles are treated as 1,3 distances.

The Ox1 structure was used as a starting model for the refinement of the Ox2 and Red1 structures. For the refinement of the Red2 structure, the refined Red1 structure was used. In all cases, σ_A (48) weighted $2|F_o| - |F_c|$ maps were calculated after each cycle, and the models were checked and adjusted in density where necessary. All electron density calculations and model manipulations were done with the Xtalview suite of programs (49). The side chain of Lys⁸⁴ was modeled and refined in two conformations in the Ox1 and Ox2 structures, but in just one conformation in the reduced structures. Glu¹⁸ was modeled in two conformations in the Red2 structure. In the second and third cycles, H₂O molecules were added and adjusted in the models, and the structures were refined with anisotropic B values. In the last cycle, hydrogen atoms were included and refined with

Table 3: Independent Derivation of Standard Deviations for the [3Fe-4S]⁰ Cluster^a

bond	Red1 ^b	su ^b	randomized ^c	SD ^d
Fe1–S2	2.23	0.019	2.22	0.004
–S3	2.24	0.017	2.25	0.006
–S4	2.23	0.017	2.24	0.003
–S γ 8	2.26	0.016	2.31	0.007
Fe2–S1	2.32	0.019	2.32	0.006
–S3	2.21	0.018	2.23	0.005
–S4	2.32	0.017	2.31	0.004
–S γ 16	2.30	0.019	2.30	0.004
Fe3–S1	2.29	0.018	2.28	0.005
–S2	2.20	0.019	2.23	0.004
–S4	2.33	0.019	2.35	0.006
–S γ 49	2.28	0.020	2.30	0.005
average	2.27	0.018	2.28	0.004
Fe1–Fe2	2.73	0.013	2.72	0.005
Fe1–Fe3	2.65	0.013	2.67	0.004
Fe2–Fe3	2.65	0.015	2.63	0.004
average	2.68	0.014	2.67	0.004

^a All values in angstroms. ^b Reduced structure refined against 1.40 Å data (Table 2). su values derived from least-squares analysis (22). ^c Average bond length resulting from refinement of 15 randomized coordinate sets against the 1.40 Å data (see Experimental Procedures). ^d Standard deviation in the bond length calculated from the 15 models resulting from refinement of randomized coordinate sets against the 1.40 Å Red1 data.

isotropic B values. Following the last cycle, standard uncertainties (su) were derived for the atomic positions from a block diagonal matrix least-squares calculation that included positional parameters but not thermal parameters. For this calculation, restraints on all protein as well as Fe, S, and S γ atoms were relaxed to yield unbiased su values. Exclusion of the thermal parameters did not lead to underestimation of the su values, but it did allow for a significant reduction in computational time. In a trial calculation using the Ox1 data that included both positional and thermal parameters in the block diagonal matrix, the derived su values differed by less than 0.1% from those obtained when the thermal parameters were excluded. Statistics for the four refined structures are summarized in Table 2. The electron density map calculated with coefficients $2|F_o| - |F_c|$ and data for the Red1 structure at 1.40 Å resolution is shown in Figure 1 in the region of the reduced [3Fe-4S]⁰ cluster. It was not possible to calculate a difference Fourier map (coefficients $|F_o| - |F_c|$) between the oxidized and reduced FdI data sets due to the change in cell constant for the c axis (Table 1), an artifact of the crystal freezing process.

To confirm that the refinement procedure is robust and not subject to bias from the input model, the following computational experiment was done. The coordinates of the model, including all protein, Fe, S, and solvent atoms, were randomly displaced by 0.25 Å rms using a Gaussian random number generator. This randomly displaced coordinate set was then refined against the 1.40 Å Red1 data set using Shelx-97 as described above. This procedure and refinement was then repeated 14 more times, yielding 15 refined coordinate sets, each derived from a differently randomized structure. The average structure of the [3Fe-4S]⁰ cluster obtained from these 15 refinement calculations is virtually identical to the one obtained initially (the Red1 structure) (Table 3). Using the 15 independently refined structures, standard deviations were derived for the Fe–S bond lengths,

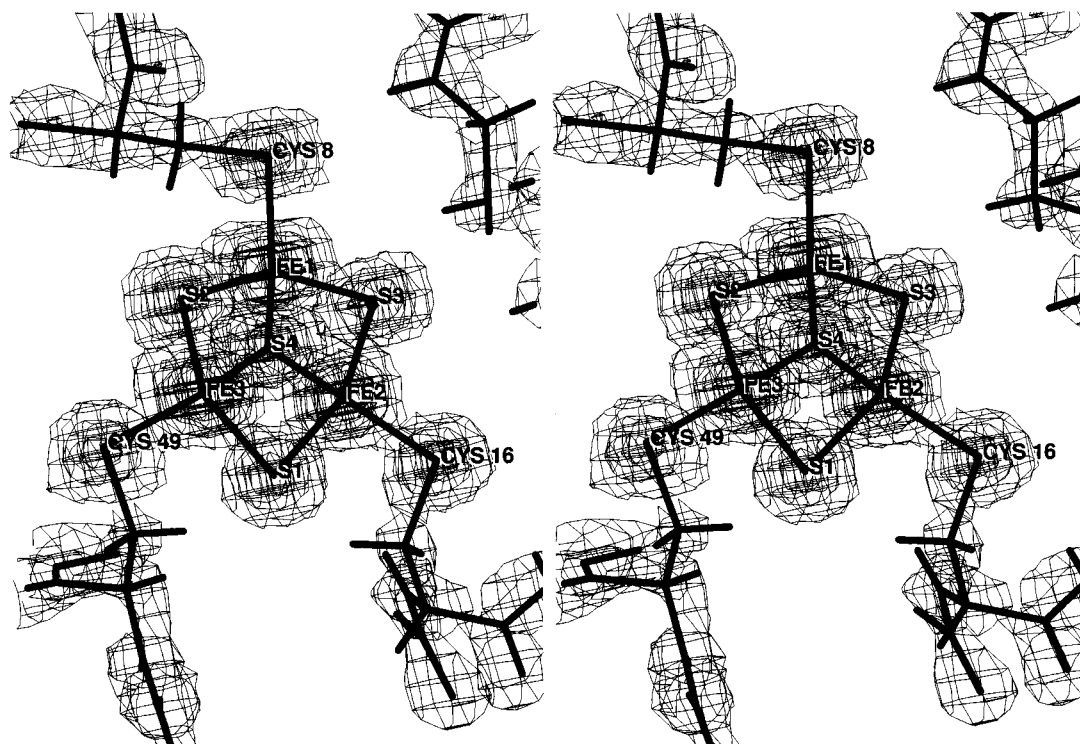


FIGURE 1: Electron density for the reduced $[3\text{Fe-4S}]^0$ cluster in the Red1 structure. The map is calculated using coefficients $2|F_o| - |F_c|$, all data in the resolution range 38.7–1.40 Å, and phases based on the final model (Table 2). The map is contoured at 2, 6, 10, and 14σ . The orientation of the cluster is the same as in Figure 3.

and they are less than the standard uncertainties (*su* values) derived from the least-squares analysis. Therefore, the derived Fe–S bond lengths are a property of the data and not the starting model. In the test case, the standard deviations for Fe–S bonds are 0.003–0.007 Å while the *su* values are 0.008–0.011 Å using the Red1 data set (Table 3). This result demonstrates that the refinement procedure is robust, that the structure converges to a set of atomic positions independent of the starting model, and that the coordinates obtained for the reduced $[3\text{Fe-4S}]^0$ cluster (Red1, Red2 structures) are not biased by the starting coordinates used. Essentially the same approach was used to evaluate the accuracy of *su* values for the $[4\text{Fe-4S}]^{2+}$ clusters in *Clostridium acidurici* refined at 0.94 Å resolution (23).

RESULTS AND DISCUSSION

Three new high-resolution structures of FdI have been refined for comparison with one previously determined high-resolution structure. Together, the four structures comprise two of the oxidized protein containing a $[3\text{Fe-4S}]^+$ cluster (Ox1, Ox2) and two of the reduced protein containing a $[3\text{Fe-4S}]^0$ cluster (Red1, Red2). Data collection for the Ox2, Red1, and Red2 structures was done using a conventional X-ray source and fine slicing during data acquisition, resulting in data of comparable quality to those collected at a synchrotron source for the Ox1 data (Table 1). All four data sets were collected from crystals frozen at 100 K. The pH of the crystals was 7.8 for the Ox1 data set and 8.5 for the Ox2, Red1, and Red2 data sets. The structures have been refined to a common resolution of 1.4 Å using a full-matrix least-squares refinement method without geometric restraints on the [Fe–S] clusters that results in *su* values for Fe–S bonds of ~ 0.01 Å (22) (Table 2). Refinement of 15 randomized models against the Red1 data demonstrates that the refine-

ment procedure is robust; i.e., the resulting structure is determined by the data and not biased by the starting model (Table 3). Furthermore, the test case demonstrates that the standard deviations due to the refinement method are smaller than the *su* values derived from the data (Table 3), indicating that the errors are not underestimated.

Summary. The results permit three types of comparisons to be made: Ox1 vs Ox2, Red1 vs Red2, and Ox1 vs Red1. The first two comparisons address the reproducibility of the data collection and refinement methods, and of the derived structures, for each oxidation state; the latter comparison addresses the effect of reduction on the $[3\text{Fe-4S}]^{+/0}$ cluster and the protein for the structures refined against the two best data sets. These comparisons lead to three conclusions. First, the structures of the $[3\text{Fe-4S}]^+$ and $[3\text{Fe-4S}]^0$ clusters are essentially the same within experimental error, suggesting that the protein may be enforcing an entatic state upon this cluster. Second, the structure of the $[3\text{Fe-4S}]^0$ cluster displays significant distortions with respect to the $[\text{Fe}_3\text{S}_4]^0$ synthetic analogue (19), further suggesting that the observed $[3\text{Fe-4S}]^{+/0}$ geometry may represent an entatic state. Third, conformational change in the protein at Asp¹⁵, as previously observed (15), and at Lys⁸⁴, resolved at 1.4 Å, together with the presence of ordered H₂O molecules in reduced FdI, implies a mechanism for H⁺ transfer to the $[3\text{Fe-4S}]^0$ cluster in agreement with electrochemical and spectroscopic results (43–45).

Evidence for Oxidized, Reduced Crystals. Following data collection, the crystal used for the Red1 data set was transferred from the 100 K N₂ gas stream to liquid N₂ without thawing and subsequently used to record EPR spectra as described under Experimental Procedures. The crystal showed no $g = 2.01$ signal whatsoever (Figure 2) for the $[3\text{Fe-4S}]^+$ cluster (35), indicating that it was essentially 100% in the

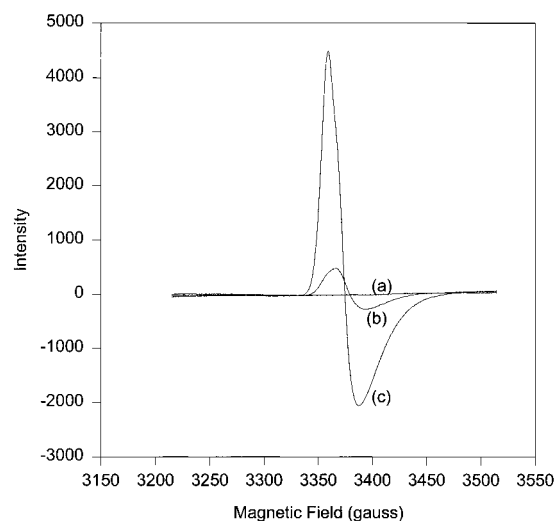


FIGURE 2: EPR spectra recorded from a FdI single crystal used for data collection (Red1 data set; Tables 1, 2). (a) The crystal after data collection and subsequent storage in liquid N₂. (b) The crystal after exposure to air for 2 min, showing partial recovery of the $g = 2.01$ signal for the [3Fe-4S]⁺ cluster. (c) The crystal after exposure to air for 2 h, showing complete recovery of the $g = 2.01$ signal. The spectrum in (c) was comparable in amplitude to similarly sized crystals of fully oxidized FdI.

[3Fe-4S]⁰ form during data collection. Upon thawing to room temperature and exposure to air for 2 min, the $g = 2.01$ began to appear; after 2 h, the signal was fully recovered (Figure 2), indicating that the integrity of the [3Fe-4S]⁺ cluster in the crystal had not been affected by treatment with sodium dithionite or by X-ray irradiation. As discussed below, the Red1 structure displays distinct conformational changes at Asp¹⁵ and Lys⁸⁴ compared to the Ox1 and Ox2 structures. Because the Red2 structure also displays these

changes, and because the crystals used for the Red1 and Red2 data sets were treated identically, it is assumed that the Red2 structure also represents the fully reduced, [3Fe-4S]⁰ state of FdI.

The crystals used for the Ox1 and Ox2 data sets were handled aerobically and not treated with sodium dithionite at any time. To test that the Ox2 crystal was not photoreduced during X-ray irradiation for 10 days, the crystal was transferred from the 100 K N₂ gas stream to liquid N₂ and used to record EPR spectra as for the Red1 crystal. If the crystal had become photoreduced, then the reduced state of the [3Fe-4S]⁰ cluster could be expected to be maintained in the N₂ gas stream at 100 K during data collection, as it was for the Red1 crystal. However, the intensity of the $g = 2.01$ signal for this crystal was identical before and after reoxidation in air for 2 h (data not shown), indicating that no photoreduction had occurred. The crystal used for the Ox1 data set was exposed to a more intense X-ray beam at a shorter wavelength (Table 1). However, the Ox1 structure displays the same conformations of Asp¹⁵ and Lys⁸⁴ as the Ox2 structure, consistent with both structures representing the oxidized state of FdI. Solution samples of cytochrome *c* oxidase irradiated for up to 2 h at room temperature with X-rays from a conventional source (1.47 Å) and a synchrotron source (1.39–1.74 Å) are also not photoreduced, as indicated by EPR and optical spectroscopy (50).

[3Fe-4S]⁺ vs [3Fe-4S]⁰. Fe–S bonds, Fe–Fe distances, and their *su* values for the [3Fe-4S]⁺⁰ clusters are summarized in Table 4. A schematic of the [3Fe-4S]⁺⁰ cluster structure with distances and angles from the Red1 structure is shown in Figure 3. The *su* values for Fe–S bonds for the Ox2 structure are only slightly larger than for the Ox1 structure, showing that data of comparable quality can be

Table 4: [3Fe-4S]⁺⁰ Cluster Geometry

distance	distances, <i>su</i> in Å				
	oxidized 1 (Ox1) ^a	oxidized 2 (Ox2)	reduced 1 (Red1)	reduced 2 (Red2)	model compound [Fe ₃ S ₄] ⁰ ^b
Fe1–S2	2.21	2.24	2.23	2.28	2.242
–S3	2.23	2.19	2.24	2.24	2.265
–S4	2.27	2.26	2.23	2.23	2.273
–Sγ8	2.29	2.24	2.26	2.26	2.310
Fe2–S1	2.28	2.25	2.32	2.32	2.275
–S3	2.29	2.23	2.21	2.27	2.250
–S4	2.32	2.29	2.32	2.30	2.333
–Sγ16	2.31	2.26	2.30	2.34	2.327
Fe3–S1	2.28	2.23	2.29	2.35	2.274
–S2	2.21	2.21	2.20	2.24	2.251
–S4	2.33	2.29	2.33	2.24	2.310
–Sγ49	2.32	2.27	2.28	2.31	2.316
average	2.28	2.25	2.27	2.28	2.286
SU (range)	0.0081–0.0111	0.0112–0.0142	0.0169–0.0196	0.0258–0.0325	0.002–0.003
SU (average)	0.0097	0.0126	0.0181	0.0295	0.0026
Fe1–Fe2	2.73	2.70	2.73	2.72	2.731
Fe1–Fe3	2.67	2.66	2.65	2.64	2.712
Fe2–Fe3	2.64	2.64	2.65	2.64	2.665
average	2.68	2.67	2.68	2.66	2.703
SU (range)	0.0059–0.0074	0.0090–0.0107	0.0125–0.0148	0.0193–0.0227	0.002–0.002
SU (average)	0.0065	0.0097	0.0136	0.0206	0.002

^a Reference 22. ^b Reference 19; Fe and S atoms renumbered for comparison as follows: the [3Fe-4S]⁰ and [Fe₃S₄]⁰ clusters were superposed on their μ₃S atoms, and the [Fe₃S₄]⁰ cluster was rotated 120° to make the longest Fe–Fe distances coincide, i.e., 2.73 and 2.73 Å. The corresponding atoms as labeled in Figure 2 and ref 19 are therefore [3Fe-4S]⁰: Fe1, Fe2, Fe3, S1, S2, S3, S4, Sγ8, Sγ16, Sγ49; and [Fe₃S₄]⁰: Fe2, Fe3, Fe1, S2, S3, S4, S1, S21, S31, S11.

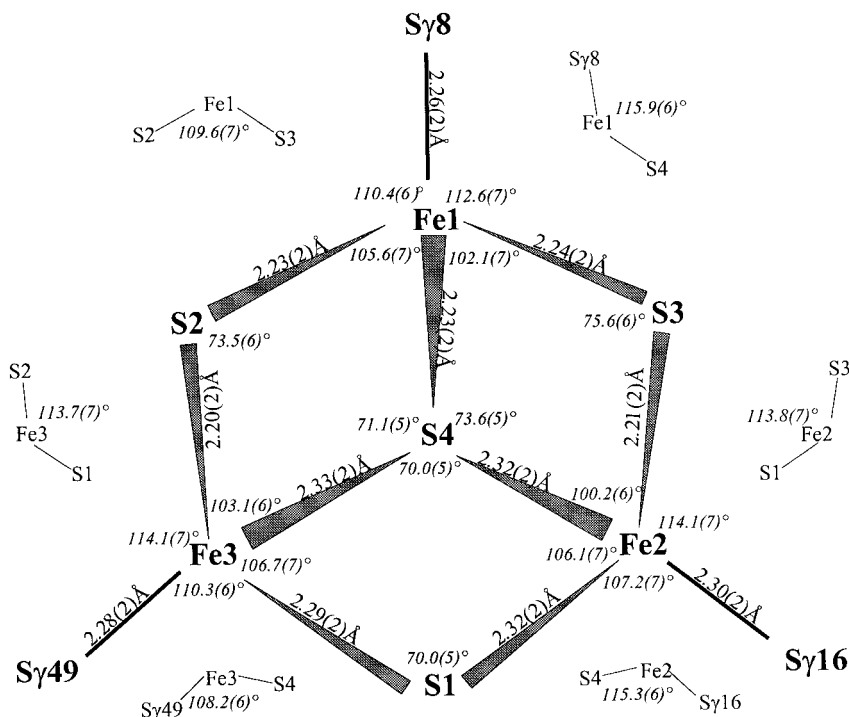


FIGURE 3: Schematic diagram of the structure and atom labeling for the $[3\text{Fe-4S}]^{+0}$ cluster in FdI with bond lengths, angles, and su values determined for the Red1 structure (Tables 3, 4).

collected with a conventional X-ray source vs a synchrotron source, although a much longer time for data collection is required. The Ox1 and Ox2 structures show that the $[\text{Fe-S}]$ cluster structure can be determined with an accuracy of $\sim\pm 0.01$ Å in completely independent experiments. In comparing these two experiments, the accuracy is $\sim\pm 0.02$ Å for Fe-S bonds; of the 12 Fe-S bonds, 7 agree within 2 times this range ($|0.04|$), and 5 differ by $|0.05|$ – $|0.06|$ Å. The Fe-Fe distances, which are more accurately determined, agree better, indicating that the larger differences in Fe-S bonds may be statistical outliers.

Within the range of accuracy defined by the su values, the $[3\text{Fe-4S}]^+$ and $[3\text{Fe-4S}]^0$ clusters do not differ significantly in structure. For the Red1 and Red2 structures, the su values are slightly larger due to the lower effective resolution and lesser completeness of these data sets (Table 1); apparently, treatment with sodium dithionite is somewhat deleterious to the crystals. Nevertheless, 10 of the Fe-S bonds in the better determined Red1 structure agree within $|0.04|$ Å, i.e., $\pm 2su$, from the mean of their values for the Ox1 and Ox2 structures; the Fe2-S1 bond is 0.05 Å longer and the Fe2-S3 bond is 0.05 Å shorter (Table 3). Despite these two differences, other metric parameters indicate that the $[3\text{Fe-4S}]^0$ and $[3\text{Fe-4S}]^+$ clusters have essentially the same structure within the accuracy of the experiments. In particular, the more accurately determined Fe-Fe distances agree within $|0.02|$ Å in all four structures (Table 4). Further, least-squares superposition of the $[3\text{Fe-4S}]$ cores results in rms deviations of 0.068 Å for Ox1 vs Ox2, 0.040 Å for Red1 vs Red2, and a range of 0.043–0.065 Å for four Ox1/2 vs Red1/2 comparisons; i.e., differences between the $[3\text{Fe-4S}]^0$ and $[3\text{Fe-4S}]^+$ clusters are no greater than the experimental errors. In terms of angles, the ‘splayed’ conformation of the core is the same for the Ox1 and Red1 structures; the average $\mu_2\text{S-Fe-}\mu_2\text{S}$ and $\mu_2\text{S-Fe-}\mu_3\text{S}$ angles are 112.4° and 103.9° , respectively, in Red1 (Figure 3), and 113.3° and

103.9° , respectively, in Ox1 (22). Trends due to bond valence are also the same: the average Fe- $\mu_3\text{S}$ bond is 0.04 Å longer than the average Fe- $\mu_2\text{S}$ bond in both the Ox1 and Red1 structures.

Based on the above metric parameters and comparisons, it can be concluded that the structure of $[3\text{Fe-4S}]^+$ cluster in FdI does not change significantly upon reduction, implying that the protein restrains its configuration. The previously reported (15) apparently larger differences between the $[3\text{Fe-4S}]^{+0}$ clusters for crystals at ambient temperature and at pH 8 must have been an artifact of the lower resolution (1.9–2.1 Å). Also, at lower resolution, restraints on the $[\text{Fe-S}]$ geometry were needed in refinement, and these could have introduced systematic errors in the model. Further, due to the use of restraints, no direct estimate of the errors in Fe and S atomic positions could be derived. In the present refinement calculations, the Fe and S atoms are resolved, su values are determined, and the results of two independent experiments for each oxidation state agree within the derived range of errors.

$[3\text{Fe-4S}]^0$ vs $[\text{Fe}_3\text{S}_4]^0$. The atomic resolution structure of the $[\text{Fe}_3\text{S}_4]^0$ synthetic analogue reveals asymmetry intrinsic to the inorganic core (19). For example, in the absence of a fourth Fe, the three $\mu_2\text{S}$ atoms are splayed outward so that the average $\mu_2\text{S-Fe-}\mu_2\text{S}$ angle is 112.6° vs 103.6° for the average $\mu_2\text{S-Fe-}\mu_3\text{S}$ angle. Also, Fe- $\mu_3\text{S}$ bonds are 0.05 Å longer on average than Fe- $\mu_2\text{S}$ bonds. These intrinsic asymmetries occur with virtually identical values in the $[3\text{Fe-4S}]^+$ and $[3\text{Fe-4S}]^0$ clusters in FdI (Figure 3) (22). However, previous comparison of the $[3\text{Fe-4S}]^+$ cluster in the Ox1 structure and the $[\text{Fe}_3\text{S}_4]^0$ synthetic analogue (22) indicated that the protein-bound cluster displays distortions not intrinsic to the core itself. The fact that the reduced $[3\text{Fe-4S}]^0$ cluster in the Red1 structure is virtually unchanged confirms this result, and it shows that the protein distorts the $[3\text{Fe-4S}]^0$ cluster relative to the synthetic analogue in the same

Table 5: [4Fe-4S]²⁺ Cluster Geometry

bond	distances, <i>su</i> in Å				cluster I ^b	cluster II ^b
	oxidized 1 (Ox1) ^a	oxidized 2 (Ox2)	reduced 1 (Red1)	reduced 2 (Red2)		
Fe1–Fe2	2.73	2.71	2.76	2.75	2.760	2.690
Fe1–Fe3	2.75	2.70	2.75	2.76	2.719	2.710
Fe1–Fe4	2.78	2.73	2.79	2.78	2.698	2.717
Fe2–Fe3	2.76	2.75	2.77	2.72	2.779	2.730
Fe2–Fe4	2.77	2.74	2.78	2.74	2.713	2.722
Fe3–Fe4	2.73	2.71	2.72	2.73	2.685	2.752
average	2.75	2.72	2.76	2.75	2.726	2.720
SU (range)	0.0060–0.0074	0.0086–0.0104	0.0123–0.0142	0.0188–0.0259	0.002–0.002	0.002–0.003
SU (average)	0.0067	0.0085	0.013	0.022	0.002	0.002

^a Reference 22. ^b Clusters I and II are [4Fe-4S]²⁺ clusters in the structure of *Clostridium acidurici* ferredoxin refined at 0.94 Å resolution (23). Cluster I has ligands Cys⁸, Cys¹¹, Cys¹⁴, and Cys⁴⁷ to Fe1, Fe2, Fe3, and Fe4, homologous with ligands Cys⁸, Cys¹⁶, and Cys⁴⁹ to the [3Fe-4S] cluster (Figure 3). Cluster II has ligands Cys¹⁸, Cys³⁷, Cys⁴⁰, and Cys⁴³ to Fe1, Fe2, Fe3, and Fe4 which have been renumbered to correspond to the FdI [4Fe-4S]²⁺ homologous ligands Cys²⁰, Cys³⁹, Cys⁴², and Cys⁴⁵ to Fe1, Fe2, Fe3, and Fe4 (22).

oxidation state. This is particularly evident in the Fe–Fe distances (Table 4). Whereas the synthetic [Fe₃S₄]⁰ cluster has two long and one short Fe–Fe distance, the protein-bound [3Fe-4S]⁺⁰ clusters have two short and one long Fe–Fe distance. The change in geometry is primarily due to a large difference in one such distance. The Fe1–Fe3 distance, with an average length of 2.66 Å in the best determined Ox1, Ox2, and Red1 structures, is shorter by more than 0.05 Å compared to the corresponding 2.712 Å distance in the [Fe₃S₄]⁰ cluster. A difference of 0.05 Å is 5 times the derived *su* values of ~0.01 Å for Fe–Fe distances in these structures. The Fe1–Sγ8 and Fe3–S2 bonds are also significantly shorter in the protein-bound clusters than in the synthetic analogue.

From these results, it is apparent that the protein distorts the [3Fe-4S]⁰ cluster relative to the geometry of the [Fe₃S₄]⁰ core bound to a symmetrical tripodal thiolate ligand. This observation, and the fact that the [3Fe-4S]⁺ and [3Fe-4S]⁰ clusters have the same structure, suggests that the conformation of the [3Fe-4S]⁺⁰ cluster in FdI may represent an entatic state. An entatic state for the [3Fe-4S]⁺⁰ cluster in FdI could be expected to facilitate the rate of electron transfer as it does for the blue Cu center in plastocyanin (9).

[4Fe-4S]²⁺ Clusters. The [4Fe-4S]²⁺ cluster in FdI has a potential of –650 mV and is not reduced by sodium dithionite at pH 8.5 (33). Consequently, the geometry of this cluster could be expected to be the same in the four independently refined structures within the limits of the experimental errors. Out of 24 possible Fe–Fe distances, all but 3, each involving Fe1 in the Ox2 structure, are the same within the ranges of *su* values (Table 5). In six pairwise least-squares superpositions, the rms deviations between [4Fe-4S]²⁺-derived structures range from 0.043 to 0.070 Å, independent of oxidation state of the [3Fe-4S]⁺⁰ cluster. The range and magnitude of these values are no different than those for the superposed [3Fe-4S]⁺⁰ clusters. This reproducibility is remarkable in light of the ~1 Å change in the unit cell *c* axis due to freezing artifacts (Table 1). The similarity of the [4Fe-4S]²⁺ cluster structures confirms the reproducibility of the refinement results and the similarity of the [3Fe-4S]⁺ and [3Fe-4S]⁰ clusters. This in turn highlights the difference between the [3Fe-4S]⁺⁰ FdI and [Fe₃S₄]⁰ synthetic clusters.

The [4Fe-4S]²⁺ cluster in FdI exhibits tetragonal distortion as observed in synthetic [Fe₄S₄]²⁺ clusters (17, 22). In

reduced [Fe₄S₄]⁺ cluster synthetic analogues, the fine details of the core geometry vary in response to extrinsic factors and affect the ground spin state (51). In the Ox1 structure, the [4Fe-4S]²⁺ cluster is compressed along one of three cluster pseudo-4-fold axes by 0.03 Å (22). The most significant compression occurs along the same axis in the Ox2, Red1, and Red2 structures (0.02, 0.04, and 0.06 Å, respectively). This result independently confirms the similarity of the [4Fe-4S]²⁺ cluster in all four refined structures. Tetragonal distortion occurs for one of the [4Fe-4S]²⁺ clusters (cluster II) in the 0.94 Å resolution structure of *Clostridium acidurici* Fd (23). In this case, the compression is 0.051 Å, and interestingly it occurs in the same direction as in FdI, suggesting that the homologous protein environments induce this cluster configuration. In FdI, the opposite faces of the [4Fe-4S]²⁺ cluster normal to the axis of compression stack on Phe² (Cys³⁹ and Cys⁴⁵ ligands) and Pro²¹ (Cys²⁰ and Cys⁴² ligands); in *C. acidurici* Fd, the opposite faces of the cluster stack on the homologous residues Tyr² (Cys³⁷ and Cys⁴³ ligands) and Pro¹⁹ (Cys¹⁸ and Cys⁴⁰ ligands). It is unlikely, however, that this common geometric feature plays a role in determining the cluster reduction potential, due to the large difference in potential between the two proteins (–650 mV vs –420 mV).

Oxidized and Reduced FdI. The [3Fe-4S]⁺⁰ cluster, its Cys ligands, and the binding loop of residues 8–16 in the Ox1, Ox2, Red1, and Red2 structures are superposed in Figure 4. The [3Fe-4S]⁺⁰ clusters and Sγ ligand atoms superpose very closely. The protein portions of these structures are also very similar, but with key differences at specific residues proximal to the [3Fe-4S]⁺⁰ cluster. Overall, the rms deviations in six pairwise least-squares superpositions of the four FdI structures range from 0.18 to 0.42 Å for all atoms, and from 0.09 to 0.12 Å for main chain N, Cα, C, and O atoms. Differences between oxidized vs reduced structures are no greater than between the independently determined oxidized or reduced structures. However, there are distinct differences at Asp¹⁵ and Lys⁸⁴, and to a lesser extent at Tyr¹³ and Thr¹⁴, and these are consistently observed in the Ox1 and Ox2 structures vs the Red1 and Red2 structures. In particular, the χ₂ torsion angle of Asp¹⁵ differs so that the carboxyl group is rotated ~90° in the Red1 and Red2 structures relative to the Ox1 and Ox2 structures. Associated with this conformational change there is a small change in the φ angle for Asp¹⁵ affecting the carbonyl of

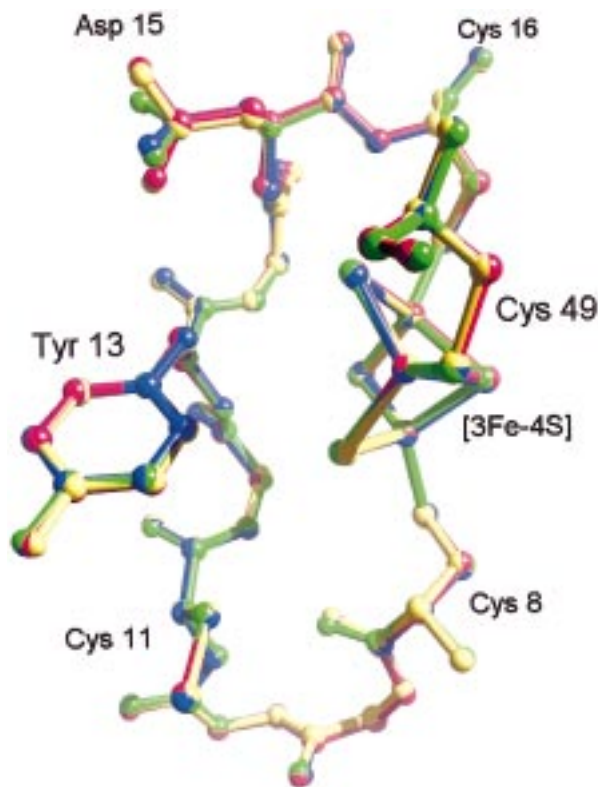


FIGURE 4: Least-squares superposition of four structures of oxidized and reduced FdI refined at 1.4 Å resolution showing main chain atoms of residues 8–16, Cys ligands, side chains of Cys¹¹, Tyr¹³, and Asp¹⁵, and the [3Fe-4S]⁺⁰ clusters. Ox1, red; Ox2, yellow; Red1, blue; Red2, green.

Thr¹⁴. Also associated with the change at Asp¹⁵ is a distinct ordering of the side chain of Lys⁸⁴, a residue in hydrogen bonding contact with Asp¹⁵. In the Ox1 and Ox2 structures, the Lys⁸⁴ side chain adopts two alternate conformations which refine with 65% and 35% relative occupancy. However, in the Red1 and Red2 structures, this side chain adopts a single conformation. $2|F_o| - |F_c|$ electron density maps at 1.4 Å resolution show the disordered density for the Lys⁸⁴ side chain in the Ox1 structure (Figure 5A) and the discretely ordered density for this side chain in the Red1 structure (Figure 5B). These maps also show the fit for the oxidized vs reduced conformations of Asp¹⁵ to the density, and the presence of additional peaks for ordered H₂O molecules in the Red1 structure. The only other significant conformational change in the reduced vs oxidized FdI structures is a 0.15 Å shift of the Tyr¹³ aromatic ring away from the [3Fe-4S]⁰ cluster (Figure 4).

Previous structural studies of oxidized and reduced FdI at pH 6 and 8 at room temperature and at 1.9–2.2 Å resolution revealed conformational changes at Asp¹⁵ consistent with increased negative charge on the [3Fe-4S]⁰ cluster but equivalent net charge on the [3Fe-4S]⁰-H⁺ cluster (15). This effect is confirmed in the 1.4 Å refined structures at pH 8.5. In the reduced state, the carboxyl group of Asp¹⁵ rotates, increasing the distance between it and the nearest μ_2 S atom of the [3Fe-4S]⁰ cluster (Figure 6). In the Ox1 structure, the shortest such distance is 4.59 Å; in the Red1 structure, it becomes 4.92 Å. Because the Asp¹⁵ side chain is solvent-exposed and expected to be ionized at pH 8.5, the conformational change is presumably due to increased electrostatic repulsion between Asp¹⁵ and the [3Fe-4S]⁰ cluster. Other

changes in FdI upon reduction can also be explained in terms of electrostatic repulsion and the new conformation of Asp¹⁵. Ordering of the Lys⁸⁴ side chain is apparently due to superior hydrogen bond geometry with Asp¹⁵ (Figure 6). Lys⁸⁴ changes conformation in the Asp¹⁵→Asn mutant of FdI as well; in this case, the side chain reorients to hydrogen bond to the carbonyl of Lys⁸⁵ in the absence of negative charge (43). In the Red1 structure, an additional H₂O molecule is ordered adjacent to Pro⁵⁰, perhaps due to improved hydrogen bonding with a H₂O in direct contact to Asp¹⁵ (Figure 6). The small shift of the aromatic ring of Tyr¹³ away from the [3Fe-4S]⁰ cluster may also be due to electrostatic repulsion. Together, the responses of the protein to the [3Fe-4S]⁰ cluster, observed in both the Red1 and Red2 structures, are consistent with the single-crystal EPR data that the cluster is indeed reduced in these structures.

NH...S Hydrogen Bonds. NH...S hydrogen bonds have long been recognized as playing a key role in selecting the oxidation states and reduction potentials of [Fe-S] clusters in proteins (52). Theoretical calculations using crystal structures and incorporating electrostatic and solvent accessibility effects show that Coulombic interactions between the protein and the [Fe-S] cluster, due in large part to amide dipoles, are a major factor in determining reduction potential (6). Decreases in average NH...S hydrogen bond length upon reduction of *Chromatium vinosum* HiPIP (13) and *Pyrococcus furiosus* Rd (14) support the hypothesis that these interactions stabilize the reduced state. In FdI, six potential NH...S hydrogen bonds occur for both the [3Fe-4S]⁺⁰ and [4Fe-4S]²⁺ clusters (Table 6). Based on *su* values, one of these, between Tyr¹³ and a μ_2 S atom of the [3Fe-4S]⁺⁰ cluster, gets significantly shorter in the Red1 structure (Figure 4). On average, there is a ~0.04 Å decrease of NH...S hydrogen bond length at the [3Fe-4S]⁺⁰ cluster vs a ~0.02 Å decrease at the [4Fe-4S]²⁺ cluster. Overall, this difference is small and not statistically significant. A lack of change in the NH...S interactions is consistent with the suggestion that the protein imposes an entatic state upon the [3Fe-4S]⁺⁰ cluster.

H⁺ Transfer to the [3Fe-4S]⁰ Cluster. Previous experiments have established that Asp¹⁵ participates directly in protonation of the [3Fe-4S]⁰ cluster in FdI to form a [3Fe-4S]⁰-H⁺ cluster (43–45). Chemical and structural arguments imply that protonation occurs at the μ_2 S atom nearest to the solvent-accessible surface of the protein. The Ox1 and Red1 structures of FdI are superposed in Figure 6. The concerted structural rearrangements that occur upon reduction suggest three specific steps of a mechanism by which a H⁺ is relayed from solvent to the S1 atom of the [3Fe-4S]⁰ cluster. First, electrostatic repulsion between the Asp¹⁵ carboxyl group and the cluster repositions the carboxyl group. Second, the side chain of Lys⁸⁴ acts as a ‘latch-key’ to capture the reduced state conformation of Asp¹⁵. As a result of improved hydrogen bond geometry between Asp¹⁵ and Lys⁸⁴, the lysine side chain becomes ordered; in contrast, it is partially disordered in the Ox1 and Ox2 structures, suggesting that the oxidized state conformations of Asp¹⁵ and Lys⁸⁴ are energetically less favorable. This situation facilitates rearrangement to the reduced state. Third, the reduced state conformation of the Asp¹⁵–Lys⁸⁴ salt bridge and the electrostatic field induced by the [3Fe-4S]⁰ cluster promote

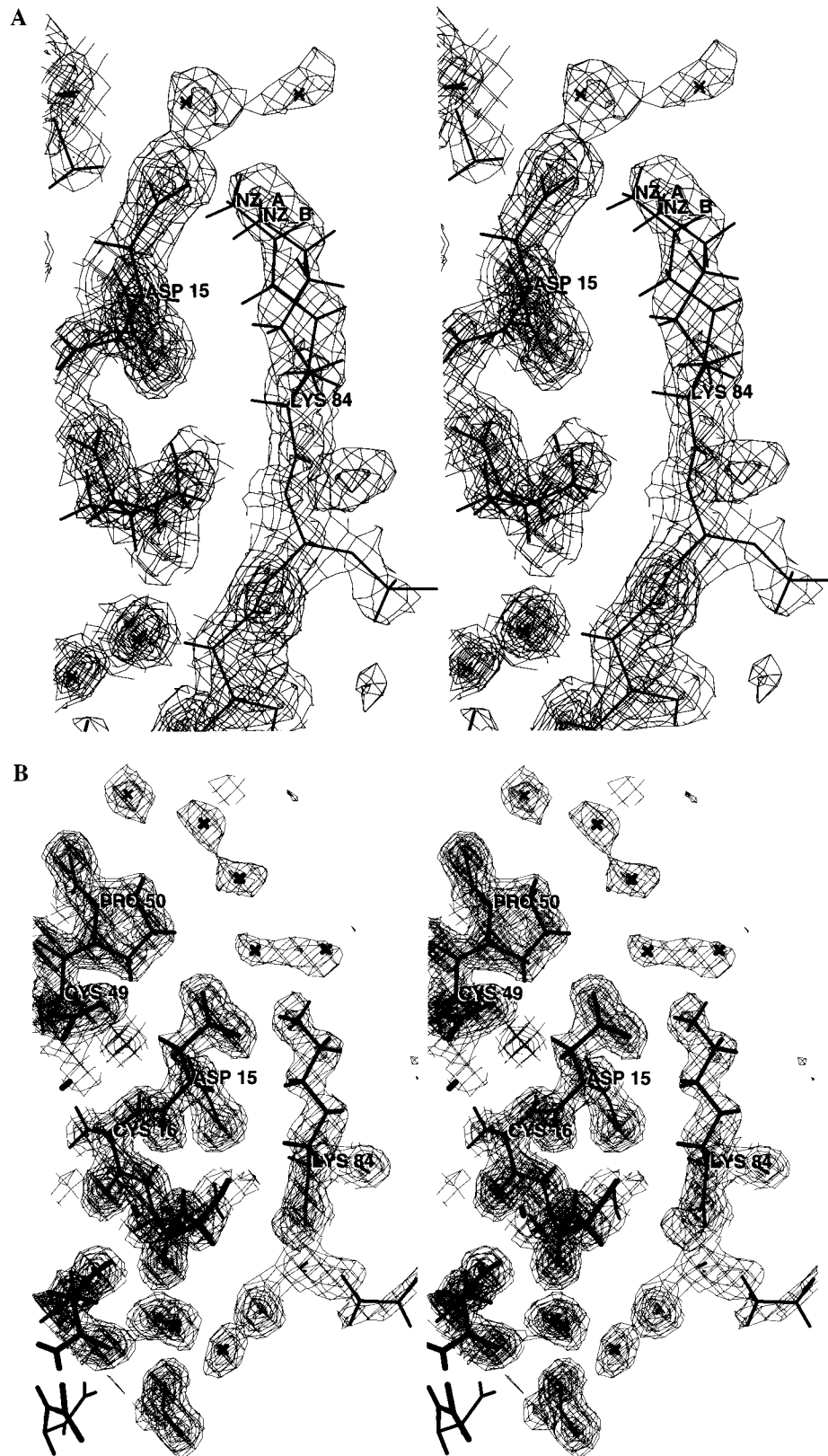


FIGURE 5: Stereo figures of the $2|F_o| - |F_c|$ electron density maps at 1.4 Å resolution showing residues at the protein surface adjacent to the [3Fe-4S]⁺⁰ cluster. (A) The Ox1 structure showing the disordered Lys⁸⁴ side chain and H₂O molecules adjacent to the Asp¹⁵–Lys⁸⁴ salt bridge. (B) The Red1 structure showing an ordered conformation for Lys⁸⁴, a new conformation for Asp¹⁵, and additional H₂O molecules adjacent to the Asp¹⁵–Lys⁸⁴ salt bridge. The maps are contoured at 1, 3, and 5 σ .

ordering of H₂O molecules at the protein surface (Figure 5A vs 5B, Figure 6), providing a source of protons.

Proton transfer from Asp¹⁵ to the [3Fe-4S]⁰ cluster is rapid, $\sim 1300 \text{ s}^{-1}$ (45), and cannot be visualized in crystal structures.

However, conformational change of Asp¹⁵ can be modeled starting from the Ox1 and Red1 FdI structures. Protonation of Asp¹⁵ from solvent in the reduced state conformation will relieve the electrostatic repulsion between it and the cluster.

Table 6: NH...S Hydrogen Bonds

hydrogen bond ^a	distances, <i>su</i> in Å				
	oxidized 1 (Ox1) ^b	oxidized 2 (Ox2)	reduced 1 (Red1)	reduced 2 (Red2)	$\langle\Delta\rangle$ (Red-Ox)
	[3Fe-4S] Cluster				
S1-N Cys ¹⁶	3.39	3.46	3.39	3.39	-0.04
S2-N Tyr ¹³	3.52	3.58	3.43	3.37	-0.15
S3-N Thr ¹⁴	3.28	3.30	3.22	3.25	-0.06
S γ 8-N Leu ³²	3.63	3.61	3.58	3.61	-0.03
S γ 49-N Ala ⁵¹	3.35	3.37	3.39	3.32	-0.01
S γ 49-N Ala ⁵³	3.40	3.38	3.46	3.37	+0.03
<i>su</i> (average)	0.03	0.03	0.05	0.08	
	[4Fe-4S] Cluster				
S1-N Ala ⁴³	3.32	3.24	3.31	3.21	-0.02
S4-N Ile ⁴⁰	3.46	3.44	3.53	3.36	-0.01
S γ 20-N Cys ²⁴	3.61	3.58	3.66	3.55	+0.01
S γ 39-N Phe ²	3.43	3.36	3.39	3.40	0.00
S γ 39-N Asp ⁴¹	3.36	3.39	3.44	3.25	-0.03
S γ 42-N Leu ⁴⁴	3.53	3.50	3.54	3.42	-0.04
<i>su</i> (average)	0.03	0.03	0.05	0.07	

^a All hydrogen bonds have N...S distances <3.60 Å in at least one structure, and all have N-H...S angles $\geq 130^\circ$. ^b Reference 22.

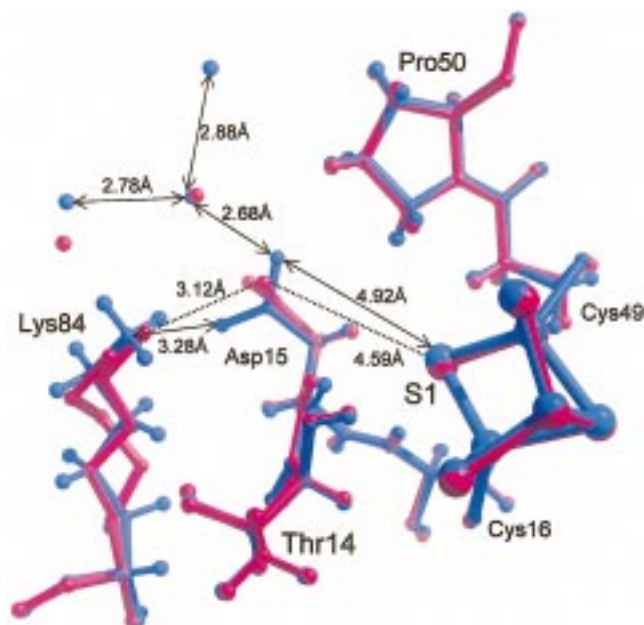


FIGURE 6: Superposition of the Ox1 (red) and Red1 (blue) structures of FdI containing [3Fe-4S]⁺ and [3Fe-4S]⁰ clusters, respectively. Residues involved in H⁺ transfer from H₂O molecules at the protein surface to S1 of the [3Fe-4S]⁰ cluster are shown along with relevant interatomic distances (Ox1 structure, dotted lines; Red1 structure, solid lines). Hydrogen atoms in the structures are shown except for the two conformers of the Lys⁸⁴ side chain in the Ox1 structure, and for H₂O molecules.

At the same time, favorable interaction with Lys⁸⁴ will be lessened. Consequently, the protonated Asp¹⁵ carboxyl group could revert to the oxidized state conformation (Figure 6). With a 180° flip of the χ_2 torsion angle, the proton would be positioned on the O δ_1 atom 4.59 Å from S1 of the cluster. If the carboxyl group is protonated at the trans lone pair nearer to S1, then given an O-H bond of ~ 0.8 Å, the H...S1 distance would be ~ 3.8 Å, almost short enough for an OH...S hydrogen bond. If H⁺ transfer does not occur via such a hydrogen bond, it could occur over an even shorter distance resulting from rotation of the Asp¹⁵ χ_1 torsion angle. Rotation of this torsion angle alone can bring O δ_1 as close as 2.04 Å of S1; however, steric clashes occur. At an O δ_1 -

S1 distance of 3.25 Å, the sum of the atomic van der Waals radii, the O δ_1 atom is 2.1–2.5 Å from hydrogen atoms on Tyr¹³ C β and Pro⁵⁰ C δ . These contacts would require a small adjustment of the protein conformation to accommodate ~ 2.6 Å van der Waals distances between O δ_1 , C β -H, or C δ -H atoms. Regardless, it is possible for Asp¹⁵ to approach sufficiently close to S1 for H⁺ transfer to occur with only small conformational changes being required. Together, these considerations based on the Ox1 and Red1 structures of FdI provide a detailed mechanism for H⁺ transfer to the [3Fe-4S]⁰ cluster.

ACKNOWLEDGMENT

We thank B. K. Burgess for protein samples, V. Sridhar and P. A. Williams for technical assistance, and J. Hirst and J. R. Williamson for helpful discussions.

REFERENCES

- Holm, R. H., Kennepohl, P., and Solomon, E. I. (1996) *Chem. Rev.* 96, 2239–2314.
- Cammack, R. (1992) *Adv. Inorg. Chem.* 38, 281–322.
- Beinert, H., Holm, R. H., and Münck, E. (1997) *Science* 277, 653–659.
- Matsubara, H., and Saeki, K. (1992) *Adv. Inorg. Chem.* 38, 223–280.
- Carrell, C. J., Zhang, H., Cramer, W. A., and Smith, J. L. (1997) *Structure* 5, 1613–1625.
- Stephens, P. J., Jollie, D. R., and Warshel, A. (1996) *Chem. Rev.* 96, 2491–2513.
- Williams, R. J. P. (1995) *Eur. J. Biochem.* 234, 363–381.
- Malmstrom, B. G. (1994) *Eur. J. Biochem.* 223, 711–718.
- Guckert, J. A., Lowery, M. D., and Solomon, E. I. (1995) *J. Am. Chem. Soc.* 117, 2817–2844.
- Peters, J. W., Stowell, M. H. B., Soltis, S. M., Finnegan, M. G., Johnson, M. K., and Rees, D. C. (1997) *Biochemistry* 36, 1181–1187.
- Musgrave, K. B., Liu, H. I., Ma, L., Burgess, B. K., Watt, G., Hedman, B., and Hodgson, K. O. (1998) *J. Biol. Inorg. Chem.* 3, 344–352.
- Carter, C. W., Jr., Kraut, J., Freer, S. T., Alden, R. A., Sieker, L. C., Adman, E. T., and Jensen, L. H. (1972) *Proc. Natl. Acad. Sci. U.S.A.* 69, 3526–3529.
- Carter, C. W., Jr., Kraut, J., Freer, S. T., and Alden, R. A. (1974) *J. Biol. Chem.* 249, 6339–6346.

14. Day, M. W., Hsu, B. T., Joshua-Tor, L., Park, J.-B., Zhou, Z. H., Adams, M. W. W., and Rees, D. C. (1992) *Protein Sci.* **1**, 1494–1507.
15. Stout, C. D. (1993) *J. Biol. Chem.* **268**, 25920–25927.
16. Berg, J. M., and Holm, R. H. (1982) *Iron–Sulfur Proteins (Metal Ions in Biology Series)* Vol. 4, pp 1–66, John Wiley and Sons, New York.
17. Holm, R. H. (1992) *Adv. Inorg. Chem.* **38**, 1–71.
18. Zhou, J., Raebiger, J. W., Crawford, C. A., and Holm, R. H. (1997) *J. Am. Chem. Soc.* **119**, 6242–6250.
19. Zhou, J., Hu, Z., Münck, E., and Holm, R. H. (1996) *J. Am. Chem. Soc.* **118**, 1966–1980.
20. Longhi, S., Czjzek, M., Lamzin, V., Nicolas, A., and Cambillau, C. (1997) *J. Mol. Biol.* **268**, 779–799.
21. Sheldrick, G. M., and Schneider, T. R. (1997) *Methods Enzymol.* **276**, 319–343.
22. Stout, C. D., Stura, E. A., and McRee, D. E. (1997) *J. Mol. Biol.* **278**, 629–639.
23. Dauter, Z., Wilson, K. S., Sieker, L. C., Meyer, J., and Moulis, J.-M. (1997) *Biochemistry* **36**, 16065–16073.
24. Bau, R., Rees, D. C., Kurtz, D. M., Jr., Scott, R. A., Huang, H., Adams, M. W. W., and Eidsness, M. K. (1998) *J. Biol. Inorg. Chem.* **3**, 484–493.
25. Kissinger, C. R., Sieker, L. C., Adman, E. T., and Jensen, L. H. (1991) *J. Mol. Biol.* **219**, 693–715.
26. Martin, A. E., Burgess, B. K., Stout, C. D., Cash, V. L., Dean, D. R., Jensen, G. M., and Stephens, P. J. (1990) *Proc. Natl. Acad. Sci. U.S.A.* **87**, 598–602.
27. Shen, B., Jollie, D. R., Stout, C. D., Diller, T. C., Armstrong, F. A., Gorst, C. M., LaMar, G. N., Stephens, P. J., and Burgess, B. K. (1994) *J. Biol. Chem.* **269**, 8564–8575.
28. Shen, B., Jollie, D. R., Diller, T. C., Stout, C. D., Stephens, P. J., and Burgess, B. K. (1995) *Proc. Natl. Acad. Sci. U.S.A.* **92**, 10064–10068.
29. Kemper, M. A., Stout, C. D., Lloyd, S. J., Prasad, G. S., Fawcett, S. E., Armstrong, F. A., Shen, B., and Burgess, B. K. (1997) *J. Biol. Chem.* **272**, 15620–15627.
30. Gao-Sheridan, H. S., Kemper, M. A., Khayat, R., Tilley, G. J., Armstrong, F. A., Sridhar, V., Prasad, G. S., Stout, C. D., and Burgess, B. K. (1998) *J. Biol. Chem.* **273**, 33692–33701.
31. Kemper, M. A., Gao-Sheridan, H. S., Shen, B., Duff, J. L. C., Tilley, G. J., Armstrong, F. A., and Burgess, B. K. (1998) *Biochemistry* **37**, 12829–12837.
32. Stout, C. D. (1989) *J. Mol. Biol.* **205**, 545–555.
33. Iismaa, S. E., Vasquez, A. E., Jensen, G. M., Stephens, P. J., Butt, J. N., Armstrong, F. A., and Burgess, B. K. (1991) *J. Biol. Chem.* **266**, 21563–21571.
34. Stephens, P. J., Jensen, G. M., Devlin, F. J., Morgan, T. V., Stout, C. D., Martin, A. E., and Burgess, B. K. (1991) *Biochemistry* **30**, 3200–3209.
35. Hu, Z., Jollie, D. R., Burgess, B. K., Stephens, P. J., and Münck, E. (1994) *Biochemistry* **33**, 14475–14485.
36. Sridhar, V., Prasad, G. S., Burgess, B. K., and Stout, C. D. (1998) *J. Biol. Inorg. Chem.* **3**, 140–149.
37. Isas, J. M., and Burgess, B. K. (1994) *J. Biol. Chem.* **269**, 19404–19409.
38. Isas, J. M., Yannoni, S. M., and Burgess, B. K. (1995) *J. Biol. Chem.* **270**, 21258–21263.
39. Prasad, G. S., Kresge, N., Muhlberg, A. B., Shaw, A., Jung, Y.-S., Burgess, B. K., and Stout, C. D. (1998) *Protein Sci.* **7**, 2541–2549.
40. Yannoni, S. M., and Burgess, B. K. (1997) *J. Biol. Chem.* **272**, 14454–14458.
41. Yannoni, S. M., and Burgess, B. K. (1998) *J. Biol. Inorg. Chem.* **3**, 253–258.
42. Jung, Y.-S., Roberts, V. A., Stout, C. D., and Burgess, B. K. (1999) *J. Biol. Chem.* **274**, 2978–2987.
43. Shen, B., Martin, L. L., Butt, J. N., Armstrong, F. A., Stout, C. D., Jensen, G. M., Stephens, P. J., LaMar, G. N., Gorst, C. M., and Burgess, B. K. (1993) *J. Biol. Chem.* **268**, 25928–25939.
44. Butt, J. N., Sucheta, A., Martin, L. L., Shen, B., Burgess, B. K., and Armstrong, F. A. (1993) *J. Am. Chem. Soc.* **115**, 12587–12588.
45. Hirst, J., Duff, J. L. C., Jameson, G. N. L., Kemper, M. A., Burgess, B. K., and Armstrong, F. A. (1998) *J. Am. Chem. Soc.* **120**, 7085–7094.
46. Howard, A. J., Nielsen, C., and Xuong, N. H. (1985) *Methods Enzymol.* **114A**, 452–472.
47. Engh, R. A., and Huber, R. (1991) *Acta Crystallogr.* **A47**, 392–400.
48. Read, R. J. (1986) *Acta Crystallogr.* **A42**, 140–149.
49. McRee, D. E. (1992) *J. Mol. Graph.* **10**, 44–47.
50. Brudvig, G. W., Bocian, D. F., Gamble, R. C., and Chan, S. I. (1980) *Biochim. Biophys. Acta* **624**, 78–89.
51. Carney, M. J., Papaefthymiou, G. C., Spartalian, K., Frankel, R. B., and Holm, R. H. (1988) *J. Am. Chem. Soc.* **110**, 6084–6095.
52. Adman, E., Watenpugh, K. D., and Jensen, L. H. (1975) *Proc. Natl. Acad. Sci. U.S.A.* **72**, 4854–4858.

BI983008I